Single-Particle Mineralogy of Chinese Soil Particles by the Combined Use of Low-Z Particle Electron Probe X-ray Microanalysis and Attenuated Total Reflectance-FT-IR Imaging Techniq...

DATASET · JULY 2015

5 **AUTHORS**, INCLUDING:

Md Abdul Malek
Inha University
**11** PUBLICATIONS   **71** CITATIONS

Single-Particle Mineralogy of Chinese Soil Particles by the Combined Use of Low-Z Particle Electron Probe X-ray Microanalysis and Attenuated Total Reflectance-FT-IR Imaging Techniques

Md Abdul Malek, BoWha Kim, Hae-Jin Jung, Young-Chul Song, and Chul-Un Ro*

Department of Chemistry, Inha University, 253, Yonghyun-dong, Nam-gu, Incheon 402-751, Korea

Ⓢ Supporting Information

ABSTRACT: Our previous work on the speciation of individual mineral particles of micrometer size by the combined use of attenuated total reflectance FT-IR (ATR-FT-IR) imaging and a quantitative energy-dispersive electron probe X-ray microanalysis technique (EPMA), low-Z particle EPMA, demonstrated that the combined use of these two techniques is a powerful approach for looking at the single-particle mineralogy of externally heterogeneous minerals. In this work, this analytical methodology was applied to characterize six soil samples collected at arid areas in

China, in order to identify mineral types present in the samples. The six soil samples were collected from two types of soil, i.e., loess and desert soils, for which overall 665 particles were analyzed on a single particle basis. The six soil samples have different mineralogical characteristics, which were clearly differentiated in this work. As this analytical methodology provides complementary information, the ATR-FT-IR imaging on mineral types, and low-Z particle EPMA on the morphology and elemental concentrations, on the same individual particles, more detailed information can be obtained using this approach than when either low-Z particle EPMA or ATR-FT-IR imaging techniques are used alone, which has a great potential for the characterization of Asian dust and mineral dust particles.
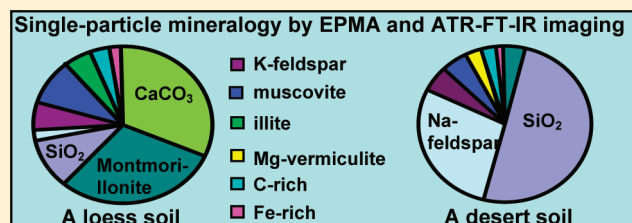
Nearly every spring, "Asian dust" originating mostly in Central China's and Mongolia's arid areas is transported into eastern China, the industrialized regions of China, and over the Yellow Sea to Korea, Japan, and even the Pacific Ocean.[1-3] Each Asian dust event can deposit a huge amount of mineral dust into the atmosphere,[4-6] and airborne mineral dust can play multiple roles in atmospheric processes.[7,8] For example, mineral dust can be an important intermediate in energy or radiation balance, cloud condensation nucleation (CCN) activities, chemical balance, and dry or wet acid deposition, and thus alter ecosystems.[9-13] The magnitude of radiation forcing or energy balance by scattering or absorbing solar radiation depends on the optical properties, like refractive index and absorption coefficients, of the dust particles, which in turn depend on their size, shape, composition, crystal structure, and the mixing state of different minerals. The CCN capacity of dust particles depends on the size distribution and swelling properties of the mineral particles.[14] The swelling and hygroscopic properties of minerals depend on their mineralogy, i.e., the extent, size, charge, or nature of the interlayer cations in their mineral structure.[15,16] Even some nonswelling minerals can possibly exhibit hygroscopic behavior when they are coated with minor, secondary hygroscopic compounds, e.g., NO_3^- and/or SO_4^{2-}, resulting from heterogeneous reactions between the mineral dust and atmospheric gaseous pollutants such as SO_x and NO_x.[17-20] Such heterogeneous reactions of mineral dust can alter the chemical balance of the atmosphere by modifying its composition.[21] Soils in different regions are enriched with

different types of minerals, some of which easily undergo secondary reactions with atmospheric gaseous pollutants while some do not. For example, calcite ($CaCO_3$) and dolomite ($CaMg(CO_3)_2$) particles can react with NO_x and/or HNO_3 to form nitrate species, whereas gypsum ($CaSO_4 \cdot 2H_2O$) does not.[6,22,23] Through long-range transport, Asian dust can reach and be deposited (wet or dry) in different remote areas like polar ice sheets, deep-sea floors, forest ranges, or cultivation fields.[24,25] Such large scale deposition can decrease ice albedo and increase solar absorption, resulting in enhanced polar ice-melt. Deposition of sulfate, phosphate and/or Na- and/or K-containing minerals (e.g., gypsum: $CaSO_4 \cdot 2H_2O$; apatite: $Ca_5(PO_4)_3(OH,F,Cl)$; feldspar: (Na,K)-$AlSi_3O_8$; muscovite: $(KAl_2(Si_3Al)O_{10}(OH,F)_2$, etc.) on the deep-sea floor can supply nutrients to oceanic floras and thus can cause enhanced eutrophication.[26] Deposition of aged, secondary SO_4^{2-} coated minerals can cause acidity in forests and crop fields adversely affecting plant growth. Thus, the impact of Asian dust can be on a global scale.[27-29]

The source regions of Asian dust particles are known to be the Yellow River basin (40°N, 100—110°E), Taklimakan desert (40°N, 80—90°E), Loess plateau (37°N, 100—115°E), and the Gobi desert (43°N, 100—110°E), all of which are high-plateau regions with an altitude of 1—2 km.[30] As the airborne dust particles are uplifted from soils at those source regions, detailed mineralogical characterization

of the source soil particles is essential to better understand the characteristics of the airborne mineral dust particles originating from those regions. In addition, the characterization of Asian dust collected at the receptor regions would possibly be useful in elucidating the influence of particular source regions on Asian dust storm episodes and the occurrence of heterogeneous reactions that might take place on the dust particles during long-range transport.

Although the numbers of studies on the chemical compositions of airborne mineral dusts originating from these source regions are continuously increasing,[2,3,31−38] just a few studies on different source soils have been reported.[22,39−41] In our previous work,[40] soil samples collected at six different arid areas of China were analyzed using a quantitative energy-dispersive electron probe X-ray microanalysis (ED-EPMA) technique, known as low-Z particle EPMA. It was observed that silicate particles among the ca. 3000 individual soil particles analyzed were most frequently encountered with the relative abundances of 30−70%, and the contents of minor elements in the silicate particles were found to be different from sample to sample, indicating that the different types of mineral species in the silicate particles could reflect the different mineralogical characteristics of the source regions. However, the low-Z particle EPMA had a limitation for the exact mineral speciation of the silicate particles as their chemical compositions and crystal structures were so diverse that the elemental concentrations obtained from X-ray spectra were not sufficient for the mineral speciation. In many cases, soil particles were internal mixtures of two or more mineral species, for which X-ray analysis is even more difficult. Recently, our group reported that the various types of individual mineral particles could be clearly identified by the combined use of two single-particle analytical techniques, i.e., low-Z particle EPMA and attenuated total reflectance Fourier transform infrared (ATR-FT-IR) imaging, where both elemental chemical compositions and mineral species can be obtained from their X-ray and ATR-FT-IR spectral data, respectively, for the same individual particles.[42−44] The recognition of the potential of this analytical approach for mineralogical characterization of individual particles prompted the investigation of the six Chinese soil samples (two from loess areas and four from desert areas) using these two techniques in combination in this work, resulting in the clear elucidation of different mineralogical characteristics of the six soil samples.

■ EXPERIMENTAL SECTION

Samples. Six soil samples, collected at various arid areas in China, were investigated in order to identify the mineral types encountered in the samples by the combined use of ATR-FT-IR imaging and low-Z particle EPMA techniques. The geographical data and sampling locations of the six soil samples can be found elsewhere.[40] The six samples are denoted by the city names of the sampling locations. The soil samples collected at the six locations are divided into two types: loess soil type is for samples Luochuan and Ganquan that were collected at the Loess plateau near the Yellow River, and sand soil type is for samples collected at the sand dunes of two different sand deserts. Samples Shaptou and Minqin were collected at the Tengger desert and samples Zangbei and Hungshan were collected at the Hungshandake desert located about 300 km north of Beijing. As large soil particles rapidly fall down nearby via gravitational settling after being uplifted into the air, and Asian dust particles are known to

be in the size range of 1 to 10 μm;[30] source soil particles of micrometer size were collected on Ag foil after grinding bulk soils and screening ground dry particles with a 20 μm sieve. Ag foil was simply rubbed over the surface of the powders, and some particles adhered to the Ag foil. About 110 individual particles for each soil sample, totaling 655 particles (<10 μm in diameter as obtained from secondary electron images (SEIs)), were analyzed.

Low-Z Particle EPMA. To obtain morphological and elemental compositional information, low-Z particle EPMA was applied for the analysis of individual soil particles prior to ATR-FT-IR imaging measurements. The measurements were carried out using a Jeol JSM-6390 scanning electron microscope (SEM) equipped with an Oxford Link SATW (Super Atmospheric Thin Window) energy dispersive X-ray (EDX) detector having a resolution of 133 eV for Mn Kα X-rays. The X-ray spectra were recorded under the control of Oxford INCA Energy software. To achieve optimal experimental conditions, i.e., low background level and high sensitivity for low-Z element analysis, an accelerating voltage of 10 kV and a beam current of 1.0 nA were used. To obtain a statistically sufficient number of counts in the X-ray spectra, a typical measuring time of 15 s for each particle was used. A more detailed discussion of the measurement conditions is given elsewhere.[45] The net X-ray intensities of the elements were obtained by nonlinear least-squares fitting of the collected spectra using the AXIL program.[46] The elemental concentrations of the individual particles were determined from their X-ray intensities by the application of a Monte Carlo calculation combined with reverse successive approximations.[45,47,48] The quantification procedure provided results accurate within 12% relative deviations between the calculated and nominal elemental concentrations when the method was applied to various types of standard particles such as NaCl, Al_2O_3, $CaSO_4 \cdot 2H_2O$, Fe_2O_3, $CaCO_3$, and KNO_3.[49,50] The low-Z particle EPMA method can provide quantitative information on the chemical composition, and the particles can be classified on the basis of their chemical species.

ATR-FT-IR Imaging Technique. ATR-FT-IR imaging measurements of individual particles were performed using a Perkin-Elmer Spectrum 100 FT-IR spectrometer interfaced to a Spectrum Spotlight 400 FT-IR microscope. For ATR imaging, an ATR accessory employing a germanium hemispherical internal reflection element (IRE) crystal with a diameter of 600 μm was used. The ATR accessory is mounted on the $X-Y$ stage of the FT-IR microscope, where contact between the sample and the IRE crystal is ensured using a force lever. A description of the sample scanning or the measuring procedure can be found elsewhere.[42,43] A spatial resolution of 3.1 μm at 1726 cm^{-1} (5.79 μm) is achievable beyond the ultimate spatial resolution limit as the IRE crystal acts like a lens, condensing the IR beam when it strikes the IRE.[51] A 16 × 1 pixel mercury cadmium telluride (MCT) array detector was used to obtain FT-IR images with a pixel size of 1.56 μm. For each pixel, an ATR-FT-IR spectrum, ranging from 720 to 4000 cm^{-1} with a spectral resolution of 4 cm^{-1}, was obtained from four interferograms that were coadded and Fourier-transformed. The position of the crystal on the sample was determined using a visible light optical microscope equipped with a light-emitting diode and a charge-coupled device camera. This optical microscope provides an image of sufficient spatial resolution that helps to locate and identify the same single particles within the same image field that had been analyzed using low-Z particle EPMA before the ATR-FT-IR imaging measurement. The time required to record ATR-FT-IR

7971

dx.doi.org/10.1021/ac201956h |*Anal. Chem.* 2011, 83, 7970−7977
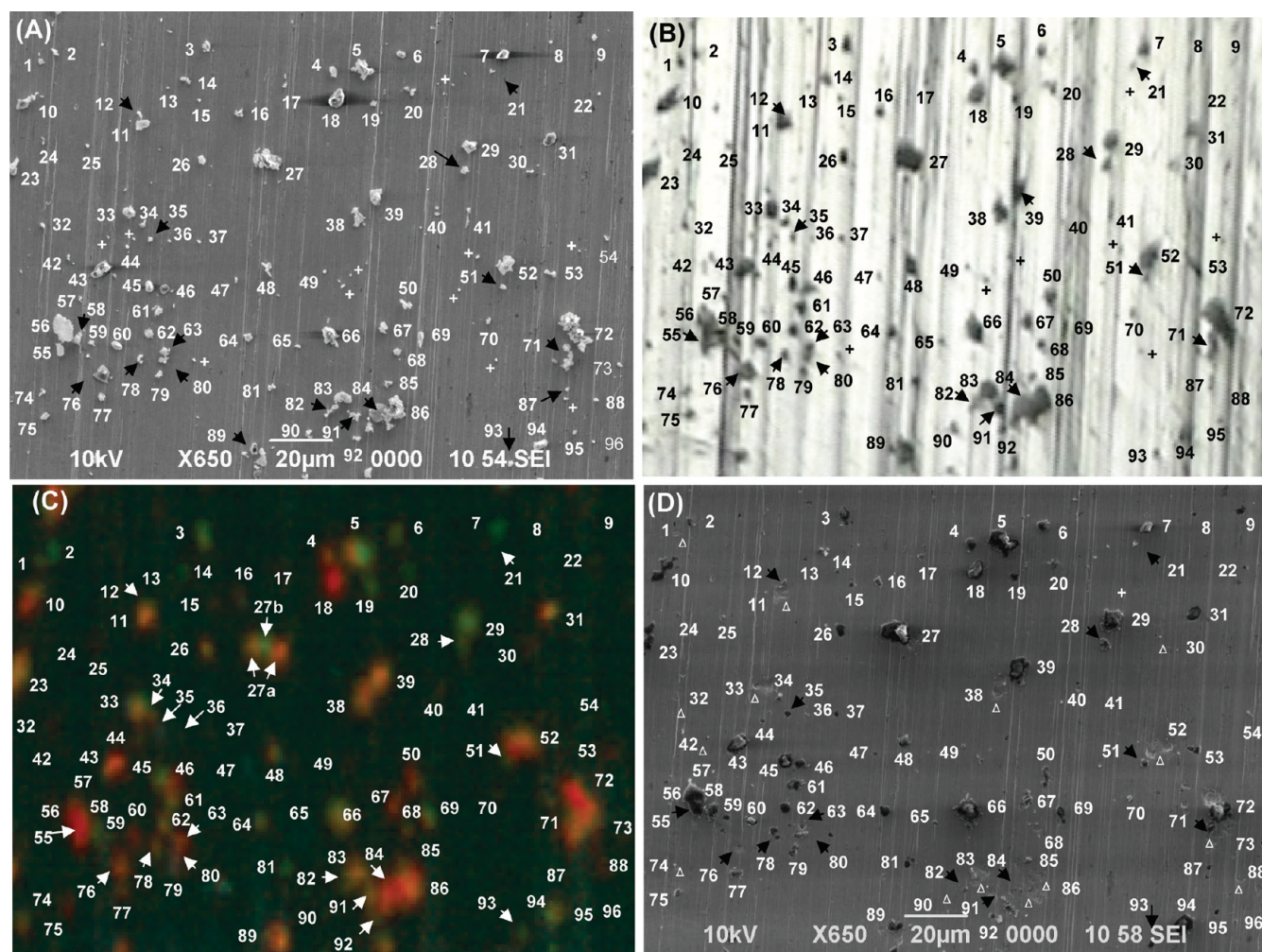
Figure 1. Secondary electron images (SEIs) (A) before and (D) after the ATR-FT-IR measurement, (B) visible light optical image, and (C) ATR-FT-IR image obtained by principal component analysis (PCA) of the same 96 individual particles of the Louchuan sample.

imaging data over $200 \times 200 \ \mu m^2$ image field with 8 scan per pixel is approximately 1 h. Spectral data processing was performed using Perkin-Elmer SpectrumIMAGE software, where images were corrected for atmospheric influences and the spectral information for each pixel was extracted by the application of principal component analysis (PCA). It is worth noticing that electron beam damage for beam sensitive particles in low-Z particle EPMA and mechanical modification of particles due to direct contact between IRE crystal and sample could happen.

■ RESULTS AND DISCUSSION

In this work, about 110 individual particles for each source soil sample, totaling 655 particles for six samples, were analyzed by the combined use of low-Z particle EPMA and ATR-FT-IR imaging techniques. As this work includes the first application of the combined technique for mineralogical characterization of soil particle samples, the unambiguous identification of mineral types present in individual soil particles will be our main concern.

Low-Z Particle EPMA and ATR-FT-IR Imaging Measurements of the Same Individual Soil Particles. Figure 1 shows SEIs, a visible light optical image, and an ATR-FT-IR image of the same 96 individual particles of Louchuan soil sample (from a

loess region) on Ag foil. Panels A and D of Figure 1 are SEIs obtained from the same image field before and after ATR-FT-IR imaging measurement. Figure 1B is a visible light optical image taken just prior to ATR-FT-IR imaging measurement, and Figure 1C is an ATR-FT-IR image. First, the morphologies and chemical compositions of all the particles on the image field were obtained using their SEIs and X-ray spectral data obtained by low-Z particle EPMA. In order to locate the same image field for ATR-FT-IR imaging measurements, visible light optical microscopy was employed to help locate the same image field previously observed using low-Z particle EPMA. After locating the same image field, the sample was made to contact the IRE crystal for ATR-FT-IR imaging measurements. The ATR-FT-IR image (Figure 1C) was obtained by the application of principal component analysis (PCA) after the first differentiation of the original ATR-FT-IR spectra for all of the pixels in the image. Although the qualities of the SEI and the ATR-FT-IR images differ due to the inherently different spatial resolutions of the images (i.e., ~100 nm for the SEI and 3.1 μm for the ATR-FT-IR image), the same patterns of particle location between the images ensure that the same particles of micrometer size were seen. Their equivalent diameters ranged from 0.94 to 8.87 μm (determined from SEI obtained before the ATR-FT-IR imaging

measurement), where the equivalent diameter was calculated by assuming that a particle with the same area for a particle on the SEI was circular. The area of each image in Figure 1 is approximately $215 \times 140 \ \mu m^2$. Considering that the pixel size of the ATR-FT-IR image is $1.56 \times 1.56 \ \mu m^2$, the number of pixels for the ATR-FT-IR image shown is $\sim$12 370. All of the pixels in the image contain full IR spectra, ranging from 4000 to 720 cm^{-1}. Although the experimental ATR-FT-IR imaging data were obtained on a $1.56 \times 1.56 \ \mu m^2$ pixel size, the manufacture's software interpolates ATR-FT-IR imaging pixel data onto a display image with more pixels, such that the final display image looks better than the actual image.

In the PCA, the ATR-FT-IR spectral data for all of the pixels in the image were considered, and similar spectra with significant encountering frequencies were grouped as a principal component. Similar minerals could be seen in the areas displayed in similar colors, and the particles composed of mixed minerals are shown in the compound color in which the major mineral leads the shade of color used. The ATR-FT-IR image (Figure 1C) indicates that six types of particles (six principal components) are dominant: carbonate particles (displayed in green: particles #2, 3, 5, 7, 29, and 81); montmorillonite particles are usually mixed with carbonate (displayed in yellow or greenish-yellow: particles #26, 33, 48, 78, and 83); muscovite particles (displayed in red: particles #18, 55, 56, 72, and 84); illite particles (displayed in orange: particles #11, 27a, 31, and 43); quartz particles (displayed in gray: particles #16, 35, 36, 79, and 80); feldspar particles (displayed in blood or dark reds: particles #67 and 75 and some of them are only weakly visible due to their small size, e.g., particles #22, 25, 44, and 95). Some particles present in the SEIs are not shown in the ATR-FT-IR image (particles #8, 9, 24, and 41, to name a few). In that case, their FT-IR spectra of the missing particles in the ATR-FT-IR image were extracted from the raw ATR-FT-IR image data at the locations known from the SEIs.

The SEIs (Figure 1A,D) clearly show the morphologies and locations of the 96 particles before and after the ATR-FT-IR imaging measurement. For the ATR-FT-IR imaging measurement, the sample has to be in contact with the IRE crystal so that some force is applied to the sample during the contact. When they are in good contact and well pressed with the IRE crystal, particles are (partly or fully) embedded into the ductile Ag collecting foil. The nonconductive mineral particles sitting on the Ag foil look bright, as shown in Figure 1A, because of their high secondary and backscattered electron yields of insulating particles, whereas the particles on the SEI taken after FT-IR measurement look dark as electrons can flow from the embedded particles into the metallic foil, resulting in low secondary and backscattered electron yields.[52] When panels A and D of Figure 1 are compared, it is clear that most particles spread out, some particles were reoriented and/or broken off into small parts, and some were missed by adhering to the IRE crystal (particles #11, 38, 52, 83, and 86, shown with triangle notations in Figure 1D). This kind of modification made between the low-Z particle EPMA and the ATR-FT-IR measurements can be easily identified by comparing two SEIs collected before and after the ATR-FT-IR imaging measurement. In addition to the inherently large spatial resolution of ATR-FT-IR imaging, the modification of particle shape owing to the contact with the IRE crystal aided broader ATR-FT-IR images of the individual particles. As the locations and sizes of all the particles in the image field are known from the SEIs, their ATR-FT-IR spectra can be extracted easily from the raw ATR-FT-IR image data. The SEIs before and after
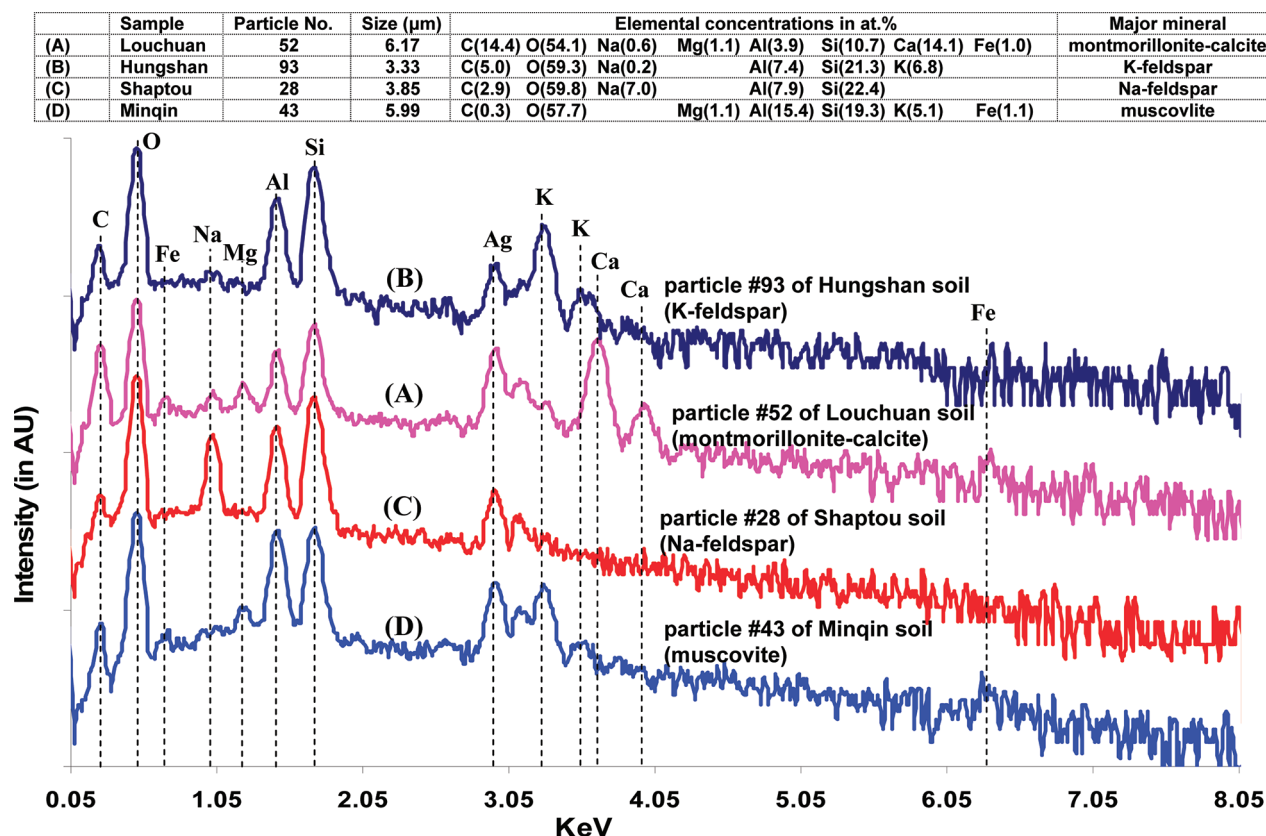
the ATR-FT-IR imaging measurement reflect the original morphology of the individual particles and the modified morphology seen during the ATR-FT-IR imaging measurement, respectively. SEIs, visible light optical images, and ATR-FT-IR images of five other samples are provided in Supporting Information.

Classification of Individual Soil Particles Based on X-ray and ATR-FT-IR Spectral Data. On the basis of the X-ray and ATR-FT-IR spectral data, overall, 15 distinct types of minerals were clearly identified as major components for the six source soil samples, which are montmorillonite, calcite, dolomite, quartz, cristobalite, Na-feldspar, K-feldspar, (Na, K)-feldspar, muscovite, illite, Mg-vermiculite, kaolinite, apatite, gypsum, and IR inactive iron oxides.

Herein is a brief summary of how the minerals were identified. The low-Z particle EPMA can provide quantitative information on the chemical composition. First, particles were regarded to be composed of only one chemical species when the chemical species constituted at least 90% in terms of the atomic fraction. Second, efforts were made to specify chemical species, even for particles internally mixed with two or more chemical species. The mixed particles were specified on the basis of all of chemical species with >10% in the formula fraction. Third, it is known that ED-EPMA has high detection limits of 0.1 to 1.0% in weight, mainly due to its high Bremsstrahlung background level. Thus, elements with less than 1.0% of atomic concentration were not included in the chemical speciation procedure. The ATR-FT-IR spectral data were used for qualitative mineral speciation and/or functional group analysis, as it is difficult to quantitatively assess mineral species of individual particles using ATR-FT-IR spectral data especially when they are internal mixtures. To specify the mineral species of individual particles using ATR-FT-IR spectral data, a homemade ATR-FT-IR spectral library was initially consulted; inorganic compounds and minerals commonly encountered in airborne particle samples were measured using ATR-FT-IR techniques to generate a custom ATR-FT-IR library. The identified mineral types of individual soil particles were cross-checked if the X-ray and ATR-FT-IR spectral data were consistent for the minerals. Detailed discussions regarding the identification of montmorillonite, feldspars, and muscovite are presented in the following sections.

Montmorillonite. Montmorillonite-containing particles are abundant in the six source soil samples (113 particles among 656; 17.2%), especially in loess Louchuan and Ganquan samples (62 particles among 223; 27.8%). The X-ray spectrum and elemental concentrations and ATR-FT-IR spectrum of a montmorillonite-containing particle, namely particle #52 of the Louchuan sample, are shown in Figures 2A and 3A, respectively. As discussed later, most of the montmorillonite-containing particles contain carbonate species. The typical example presented here for a montmorillonite-containing particle also shows a significant amount of carbonate mineral. Elemental concentrations of this particle in terms of atomic fraction are O (54%), C (14%), Si (11%), Ca (14%), Al (4%), Fe (1%), and Mg (1%), indicating the presence of aluminosilicate and $CaCO_3$ species because of the relatively high levels of Si and Al as well as Ca and C. The contents of Mg and Fe are lower than that of Al, suggesting that the major aluminosilicate mineral contains Mg and possibly Fe as minor elements. The relative atomic concentrations of Mg, Al, Si, and Fe compared to that of Mg are 1.0, 3.5, 9.7, and 1.0, respectively, which are close to the chemical compositions of montmorillonite $((0.5Ca,Na)_{0.7}(Al,Mg,Fe)_4[(Si,Al)_8O_{20}](OH)_4 \cdot nH_2O)$, except for an excess of Si, which might be due to the presence of the

7973

dx.doi.org/10.1021/ac201956h |Anal. Chem. 2011, 83, 7970–7977

|	Sample	Particle No.	Size (μm)	Elemental concentrations in at.%								Major mineral
(A)	Louchuan	52	6.17	C(14.4)	O(54.1)	Na(0.6)	Mg(1.1)	Al(3.9)	Si(10.7)	Ca(14.1)	Fe(1.0)	montmorillonite-calcite
(B)	Hungshan	93	3.33	C(5.0)	O(59.3)	Na(0.2)		Al(7.4)	Si(21.3)	K(6.8)		K-feldspar
(C)	Shaptou	28	3.85	C(2.9)	O(59.8)	Na(7.0)		Al(7.9)	Si(22.4)			Na-feldspar
(D)	Minqin	43	5.99	C(0.3)	O(57.7)		Mg(1.1)	Al(15.4)	Si(19.3)	K(5.1)	Fe(1.1)	muscovlite

Figure 2. X-ray spectra and elemental concentrations of four individual particles containing montmorillonite, Na-feldspar, K-feldspar, and muscovite as their major minerals.

small amount of silica (quartz or cristobalite) as another minor mineral. However, the identification of the silicate types just based on the elemental concentration data runs the risk of being speculative as there are many types of silicate minerals. The ATR-FT-IR spectrum of this particle, shown in Figure 3A, matches well with the library spectrum of montmorillonite (shown in an inset), where IR absorption peaks for montmorillonite are observed at 1014 cm^{-1} due to Si—O stretching, weak shoulder peak at 910 cm^{-1} due to AlAl—OH deformation, at 835 cm^{-1} due to AlFe—OH deformation, and at 796 cm^{-1} due to AlMg—OH deformation.[53] The appearance of an additional weak peak at 1162 cm^{-1} (Si—O), and a comparatively stronger peak at 796 cm^{-1} indicate the presence of a small amount of silica. It is observed that the presence of silica influences the Si—O stretching band of montmorillonite to shift slightly to a higher position, herein at 1014 cm^{-1}. The magnitude of the shift depends on the content of silica in the particles. Strong IR peaks at 1416 cm^{-1} (v_3 band), 873 cm^{-1} (v_2 band), and at 721 cm^{-1} (v_4 band) are from the CaCO$_3$ moiety,[54] supporting the presence of a significant amount of CaCO$_3$ species.

Feldspars. In Figures 2B,C and 3B,C, X-ray spectra and elemental concentrations and ATR-FT-IR spectra of a K-feldspar (#93 of the Hungshan sample) and a Na-feldspar (#28 of the Shaptou sample) particle are shown. The elemental concentrations of the K-feldspar particle in terms of atomic fraction are O (59%), Si (21%), Al (7%), C (5%), and K (7%), and those of the Na-feldspar are O (59%), Si (22%), Al (8%), Na (7%), and C (3%), indicating the presence of aluminosilicate and carbonaceous species. The relative atomic concentrations of particles

#93 and #28 are K/Al/Si = 1.0:1.1:3.1 and Na/Al/Si = 1.0:1.2:3.2, very similar to the stoichiometries of K-feldspar (KAlSi$_3$O$_8$) and Na-feldspar (NaAlSi$_3$O$_8$), respectively. However, as there are many different silicate minerals, their silicate mineral types cannot be conclusively determined solely on the basis of their elemental concentration data. When ATR-FT-IR spectral data are combined with X-ray spectral data, K-feldspar and Na-feldspar can be clearly distinguished from other silicate minerals. As shown in Figure 3B,C, ATR-FT-IR spectra of particles #93 and #28 match well with the library spectra of single component minerals of K-feldspar and Na-feldspar, respectively, shown in the left inset. Particle #93 shows 6 IR peaks at 1129, 1108, 1034, 1012, 773, and 729 cm^{-1}, whereas particle #28 shows 10 IR peaks at 1164, 1113, and 1094 cm^{-1} due to Si—O stretching, at 1035, 1003, and 977 cm^{-1} due to Si(Al)—O stretching, at 788 and 768 cm^{-1} due to Si—Si stretching, and at 746 and 721 cm^{-1} due to Si—(Al)Si stretching. Fewer IR peaks in K-feldspar than Na-feldspar are in good agreement with those reported in the other study.[55]

Muscovite. The X-ray spectrum and elemental concentrations and ATR-FT-IR spectrum of a muscovite particle, namely particle #43 of the Minqin sample, are shown in Figures 2D and 3D, respectively. The elemental concentrations of this muscovite particle are O (58%), Si (19%), Al (15%), K (5%), C (3%), Fe (1%), and Mg (1%), indicating the presence of aluminosilicate and carbonaceous species. The relative atomic concentrations of particle #43 are K/Al/Si = 1.0:3.0:3.8, similar to the stoichiometry of muscovite (KAl$_2$(Si$_3$Al)O$_{10}$(OH,F)$_2$). As shown in Figure 3D, the ATR-FT-IR spectrum of this particle matches
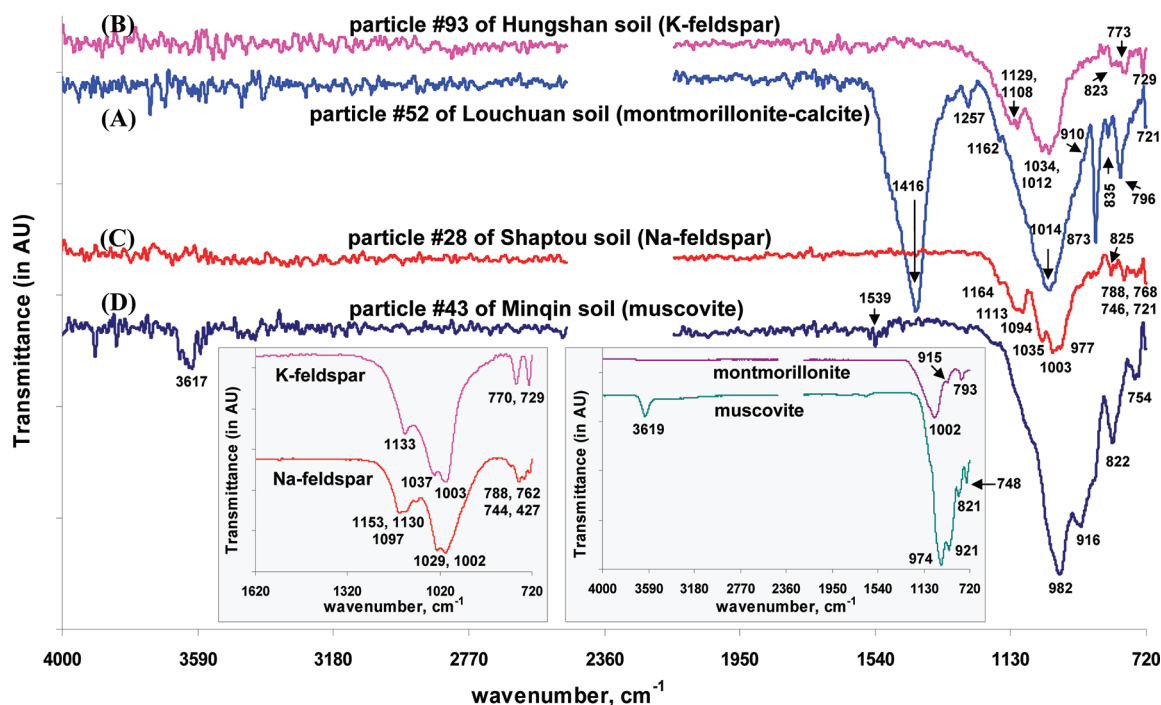
Figure 3. ATR-FT-IR spectra of four individual particles containing montmorillonite, Na-feldspar, K-feldspar, and muscovite as their major minerals. The library spectra of montmorillonite, Na-feldspar, K-feldspar, and muscovite minerals are shown in the insets.

well with the library spectrum of the single component mineral of muscovite (shown in the right inset). The pattern of the structural hydroxyl peak at 3617 cm^{-1}, the intensity of Si(Al)−O asymmetric stretching peak at 982 cm^{-1}, the staircase structure of successive peaks over 1000−750 cm^{-1}, and the presence of a characteristic peak pair at 822 and 754 cm^{-1} due to tetrahedral Al−O stretching out of plane and Al−O−Si deformation in-plane[53,56] confirm that the major mineral of this particle is muscovite. The minor Mg and Fe contents of this particle are possibly due to presence of the small amount of montmorillonite, which has similar IR peaks merged with those of muscovite.

Detailed discussions regarding the identification of the other minerals, i.e., illite, Mg-vermiculite, kaolinite, quartz, cristobalite, carbonates, elemental carbon, Fe-rich, CaSO$_4$, and TiO$_2$ particles, are presented in the Supporting Information.

Mineralogical Characteristics of Six Source Soil Samples. As shown in Table 1, the most abundant mineral encountered in the six soil samples is quartz (203 particles among overall 656; 31.0%), followed by montmorillonite (113; 17.2%), Na-feldspar (81; 12.3%), calcite (63; 9.6%), K-feldspar (44; 6.7%), and muscovite (44; 6.7%). Many particles are not in pure mineral forms, containing minor mineral types along with the major one. Herein, all the montmorillonite-containing particles mixed with minor calcite, Na-feldspar, or calcite and Na-feldspar are categorized as the particle type of montmorillonite, in order not to make a complex classification table including minor minerals.

Montmorillonite and calcite are abundant in the loess soil samples (Louchuan and Ganquan), whereas quartz and feldspars are abundant in the desert soil samples (Shaptou, Minqin, Hungshan, and Zangbei). The source regions of the airborne particles, i.e., loess or desert, can be clearly differentiated by investigating the contents of montmorillonite, calcite, quartz, and feldspars of the airborne mineral particles collected during Asian

Dust storm events. In addition, calcite is almost ubiquitously present in the silicate minerals of the loess samples. Table 2 shows the encountering probabilities of carbonate-containing silicate particles in specific types of silicate particles, where the presence of carbonate species was determined on the basis of both low-Z particle EMPA and ATR-FT-IR spectral data. For the loess soils (Louchuan and Ganquan), more than 90% of montmorillonite, muscovite, and illite contain carbonate minerals as their minor mineral, and more than 60% of quartz, crystobalite, and feldspars do. For the desert soils (Shaptou, Hungshan, and Zangbei), no silicate particles contain carbonate. The desert soil Minqin sample is different from the other desert soil samples, in that quartz, cristobalite, montmorillonite, and feldspars contain some carbonate (4−19%). This observation indicates that the almost ubiquitous presence of the carbonate species in silicate minerals is one of the characteristics of loess soils.

The two loess samples are different in their minor mineral contents; e.g., the Louchuan soil contains lower and higher levels of Na-feldspar and K-feldspar, respectively, than the Ganquan soil does (see Table 1). Illite is encountered uniquely in the Louchuan sample. The Ganquan soil possesses higher levels of carbonaceous particles than the Louchuan soil, mainly as IR inactive elemental carbon. The presence of carbonaceous species in aerosol particles is of interest as carbonaceous species can play an important role in heterogeneous atmospheric reactions and radiative forcing of aerosols.

As sand is the main component in desert soils, many of the desert soil particles are quartz and cristobalite, but their contents vary sample to sample, i.e., 47%, 47%, 61%, and 33% for Shaptou, Minqin, Hungshan, and Zangbei samples, respectively. The Zangbei sample contains a significant amount of montmorillonite. The Shaptou sample is unique for having a significant amount of Na-feldspar, whereas the Minqin and Zhangbei soils differ from other desert soil samples with respect to their significant muscovite

Table 1. Number and Relative Abundances of Major Mineral Types Encountered in Six Soil Samples

	number of particles						
	loess soils		desert soils				
major minerals identified	Luochuan	Ganquan	Shaptou	Minqin	Hungshan	Zangbei	sum
quartz (SiO_2)	10 (10.3%)	13 (10.3%)	42 (42.0%)	45 (37.8%)	60 (52.2%)	33 (33.4%)	203 (31.0%)
cristobalite (SiO_2)		1 (0.8%)	5 (5.0%)	2 (1.7%)	1 (0.9%)		9 (1.4%)
calcite ($CaCO_3$)	25 (25.7%)	33 (26.2%)		4 (3.4%)		1 (1.0%)	63 (9.6%)
dolomite ($CaMg(CO_3)_2$)	4 (4.1%)			1 (0.8%)			5 (0.8%)
montmorillonite $((0.5Ca,Na)_{0.7}(Al,Mg,Fe)_4$ $[(Si,Al)_8O_{20}](OH)_4 \cdot nH_2O)$	26 (26.8)	36 (28.5%)	4 (4.0%)	16 (13.0%)	11 (9.6%)	20 (20.2%)	113 (17.2%)
Na-feldspar ($NaAlSi_3O_8$)	2 (2.1%)	9 (7.1%)	27 (27.0%)	14 (12.0%)	14 (12.0%)	15 (15.2%)	81 (12.3%)
K-feldspar ($KAlSi_3O_8$)	5 (5.2%)	4 (3.2%)	5 (5.0%)	9 (7.6%)	11 (9.6%)	10 (10.1%)	44 (6.7%)
muscovite ($KAl_2(Si_3Al)O_{10}(OH,F)_2$)	9 (9.3%)	8 (6.4%)	5 (5.0%)	9 (7.6%)	2 (1.7%)	11 (11.1%)	44 (6.7%)
Mg-vermiculite $((Mg_{2.36}Fe_{0.48}Al_{0.16})$ $(Al_{1.28}Si_{2.72})O_{10}(OH)_2 \cdot 4.32H_2O)$		1 (0.8%)	3 (3.0%)	3 (2.5%)			7 (1.1%)
illite $((K,H_3O)(Al,Mg,Fe)_2(Si,Al)_4O_{10^-}$ $[(OH)_2,(H_2O)])$.	5 (5.2%)					1 (1.0%)	6 (0.9%)
apatite $((Ca_5(PO_4)_3(OH,F,Cl))$		1 (0.8%)					1 (0.2%)
kaolinite ($Al_4Si_4O_{10}(OH)_2$)					1 (0.9%)	1 (1.0%)	2 (0.3%)
$CaSO_4$				1 (0.8%)			1 (0.2%)
elemental carbon	3 (3.1%)	12 (9.5%)	3 (3.0%)	2 (1.7%)	3 (2.6%)	3 (3.0%)	26 (4.0%)
Fe-rich minerals	2 (2.1%)	3 (2.4%)	1 (1.0%)	7 (5.9%)	8 (7.0%)	1 (1.0%)	22 (3.4%)
NAIC[a]	6 (6.1%)	5 (4%)	5 (5.0%)	6 (5.0%)	4 (3.5%)	3 (3.0%)	29 (4.4%)
sum	97 (100%)	126 (100%)	100 (100%)	119 (100%)	115 (100%)	99 (100%)	656 (100%)

[a] NAIC: Not enough information contained in the ATR-FT-IR spectral data for identification of the mineral type.

Table 2. Number of Carbonate-Containing Silicate Particles Encountered in Specific Silicate Particles

	loess soils				desert soils							
silicate minerals	Louchuan		Ganquan		Shaptou		Minqin		Hungshan		Zangbei	
quartz/cristobalite	6/10	(60.0%)	9/14	(64.3%)	0/47	(0%)	4/47	(8.5%)	0/61	(0%)	0/33	(0%)
montmorillonite	24/26	(92.3%)	35/36	(97.2%)	0/4	(0%)	3/16	(18.7%)	0/11	(0%)	0/20	(0%)
feldspars	5/7	(71.4%)	10/13	(76.9%)	0/32	(0%)	1/23	(4.3%)	0/25	(0%)	0/25	(0%)
muscovite	9/9	(100%)	8/8	(100%)	0/5	(0%)	0/9	(0%)	0/2	(0%)	0/11	(0%)
Mg-vermiculite			1/1	(100%)	0/3	(0%)	0/3	(0%)				
illite	5/5	(100%)									0/1	(0%)
total average	49/57	(86.0%)	63/72	(87.5%)	0/91	(0%)	8/98	(8.1%)	0/99	(0%)	0/90	(0%)

contents. All desert soils contain a higher level of Na-feldspar than K-feldspar. The Minqin and Hungshan soils contain a higher level of iron oxide minerals than the Shaptou and Zhangbei soils.

Although the number of particles analyzed for each soil sample is limited in this work, our results demonstrate that each soil sample can be differentiated from the others on the basis of its single-particle mineralogy.

CONCLUSIONS

In this work, it is demonstrated that single-particle mineralogy can be performed even for internally mixed particles using a combination of ATR-FT-IR imaging and low-Z particle EPMA techniques. These two techniques provide complementary information so that elemental concentration data from low-Z particle EPMA can help to identify minerals when ATR-FT-IR spectra are not clearly indicative for the identification of certain minerals, and alternatively particles with similar elemental compositions can be identified using their different ATR-FT-IR spectra. Two different types of soils, i.e., loess and desert soils, were characterized by the

single-particle mineralogical approach. The major minerals encountered in loess soils are montmorillonite and calcite, and those in desert soils are quartz and feldspars. However, the relative abundances of major minerals and some minor minerals, e.g., muscovite, illite, and Mg-vermiculite vary from sample to sample. This single-particle mineralogy has great potential for the characterization of Asian dust aerosols, and detailed investigation of the mineralogy of source soil particles could provide an insight for tracking the source of airborne Asian dust particles in the long run.

ASSOCIATED CONTENT

S Supporting Information. Additional data in 11 figures. This material is available free of charge via the Internet at http://pubs.acs.org.

AUTHOR INFORMATION

Corresponding Author
*Tel.: +82 32 860 7676. Fax: +82 32 867 5604. E-mail: curo@inha.ac.kr.

■ ACKNOWLEDGMENT

■ REFERENCES

(1) Fairlie, T. D.; Jacob, D. J.; Park, R. J. *Atmos. Environ.* **2007**, *41*, 1251–1266.

(2) Hwang, H.; Kim, H. K.; Ro, C.-U. *Atmos. Environ.* **2008**, *42*, 8738–8746.

(3) Geng, H.; Park, Y.-M.; Hwang, H.; Kang, S.; Ro, C.-U. *Atmos. Chem. Phys.* **2009**, *9*, 6933–6947.

(4) Shao, Y.; Dong, C. H. *Global Planet. Change* **2006**, *52*, 1–22.

(5) Zhao, T. L.; Gong, S. L.; Zhang, X. Y.; Blanchet, J.-P.; McKendry, I. G.; Zhou, Z. J. *J. Climate* **2006**, *19*, 88–103.

(6) Gong, S. L.; Zhang, X. Y.; Zhao, T. L.; Zhang, X. B.; Barrie, L. A.; McKendry, I. G.; Zhao, C. S. *J. Climate* **2006**, *19*, 104–122.

(7) Dentener, F. J.; Carmichael, G. R.; Zhang, Y.; Lelieveld, J.; Crutzen, P. J. *J. Geophys. Res.* **1996**, *101*, 22869–22889.

(8) Usher, C. R.; Michel, A. E.; Grassian, V. H. *Chem. Rev.* **2003**, *103*, 4883–4939.

(9) Ge, J.; Huang, J.; Weng, F.; Sun, W. *Atmos. Chem. Phys.* **2008**, *8*, 4903–4909.

(10) Satheesh, S. K.; Moorthy, K. K. *Atmos. Environ.* **2005**, *39*, 2089–2110.

(11) Su, J.; Huang, J.; Fu, Q.; Minnis, P.; Ge, J.; Bi, J. *Atmos. Chem. Phys.* **2008**, *8*, 2763–2771.

(12) Huang, J.; Minnis, P.; Lin, B.; Wang, T.; Yi, Y.; Hu, Y.; Sun-Mack, S.; Ayers, K. *Geophys. Res. Lett.* **2006**, *33*, L06824, DOI: 10.1029/2005GL024724.

(13) Min, Q.-L.; Li, R.; Lin, B.; Joseph, E.; Wang, S.; Hu, Y.; Morris, V.; Chang, F. *Atmos. Chem. Phys.* **2009**, *9*, 3223–3231.

(14) Koehler, K. A.; Kreidenweis, S. M.; DeMott, P. J.; Petters, M. D.; Prenni, A. J.; Carrico, C. M. *Geophys. Res. Lett.* **2009**, *36*, L08805, DOI: 10.1029/2009GL037348.

(15) Schuttlefield, J. D.; Cox, D.; Grassian, V. H. *J. Geophys. Res.* **2007**, *112*, D21303, DOI: 10.1029/2007JD008973.

(16) Herich, H.; Tritscher, T.; Wiacek, A.; Gysel, M.; Weingartner, E.; Lohmann, U.; Baltensperger, U.; Cziczo, D. J. *Phys. Chem. Chem. Phys.* **2009**, *11* (36), 7804–7809.

(17) Shi, Z.; Zhang, D.; Hayashi, M.; Ogata, H.; Ji, H.; Fujiie, W. *Atmos. Environ.* **2008**, *42* (4), 822–827.

(18) Sullivan, R. C.; Moore, M. J. K.; Petters, M. D.; Kreidenweis, S. M.; Roberts, G. C.; Prather, K. A. *Atmos. Chem. Phys.* **2009**, *9*, 3303–3316.

(19) Al-Hosney, H. A.; Grassian, V. H. *Phys. Chem. Chem. Phys.* **2005**, *7*, 1266–1276.

(20) Fairlie, T. D.; Jacob, D. J.; Dibb, J. E.; Alexander, B.; Donkelaar, A. V.; Zhang, L. *Atmos. Chem. Phys.* **2010**, *10*, 3999–4012.

(21) Sullivan, R. C.; Guazzotti, S. A.; Sodeman, D. A.; Prather, K. A. *Atmos. Chem. Phys.* **2007**, *7*, 1213–1236.

(22) Krueger, B. J.; Grassian, V. H.; Cowin, J. P.; Laskin, A. *Atmos. Environ.* **2004**, *38*, 6253–6261.

(23) Li, W. J.; Shao, L. Y. *Atmos. Chem. Phys.* **2009**, *9*, 1863–1871.

(24) Ratmeyer, V.; Balzer, W.; Bergametti, G.; Chiapello, I.; Fischer, G.; Wyputta, U. *Mar. Geol.* **1999**, *159*, 241–252.

(25) Dong, Z.; Li, Z.; Edwards, R.; Wu, L.; Zhou, P. *Atmos. Res.* **2011**, *101*, 294–306.

(26) Jo, C. O.; Lee, J.-Y.; Park, K.-A.; Kim, Y. H.; Kim, K.-R. *Geophys. Res. Lett.* **2007**, *34*, L05602, DOI: 10.1029/2006GL027395.

(27) Tegen, I.; Schepanski, K. *IOP Conf. Ser.: Earth Environ. Sci.* **2009**, *7*, 012001, DOI: 10.1088/1755-1307/7/1/012001.

(28) Tegen, I. *Quat. Sci. Rev.* **2003**, *22*, 1821–1834.

(29) Zhao, C.; Liu, X.; Leung, L. R.; Johnson, B.; McFarlane, S. A.; Gustafson, W. I., Jr.; Fast, J. D.; Easter, R. *Atmos. Chem. Phys.* **2010**, *10*, 8821–8838.

(30) Chun, Y. S.; Kim, J.; Choi, J. C.; Boo, K. O.; Oh, S. N.; Lee, M. *Atmos. Environ.* **2001**, *35*, 2715–2721.

(31) Ro, C.-U.; Hwang, H.; Kim, H. K.; Chun, Y.; Van Grieken, R. *Environ. Sci. Technol.* **2005**, *39*, 1409–1419.

(32) Hwang, H.; Ro, C.-U. *Spectrochim. Acta B* **2006**, *61*, 400–406.

(33) Ganor, E.; Stupp, A.; Alpert., P. *Atmos. Environ.* **2009**, *43*, 5463–5468.

(34) Coz, E.; Gómez-Moreno, F. J.; Pujadas, M.; Casuccio, G. S.; Lersch, T. L.; Artíñano, B. *Atmos. Environ.* **2009**, *43*, 1850–1863.

(35) Choi, J. C.; Lee, M.; Chun, Y.; Kim, J.; Oh, S. *J. Geophys. Res.* **2001**, *106* (D16), 18067–18074.

(36) Zang, X. Y.; Gong, S. L.; Shen, Z. X.; Mei, F. M.; Xi, X. X.; Liu, L. C.; Zhou, Z. J.; Wang, D.; Wang, Y. Q.; Cheng, Y. *J. Geophys. Res.* **2003**, *108* (D9), 4261, DOI: 10.1029/2002JD002632.

(37) Cheng, T.; Lu, D.; Wang, G.; Xu, Y. *Atmos. Environ.* **2005**, *39*, 2903–2911.

(38) Yang, F.; Ye, B.; He, K.; Ma, Y.; Cadle, S. H.; Chan, T.; Mulawa, P. A. *Sci. Total Environ.* **2005**, *343*, 221–230.

(39) Jeong, G. Y. *J. Geophys. Res.* **2008**, *113*, D02208, DOI:10.1029/2007JD008606.

(40) Kim, H. K.; Hwang, H.-J.; Ro, C.-U. *Spectrochim. Acta B* **2006**, *61*, 393–399.

(41) Doğan, M. *Indoor Built Environ.* **2003**, *12*, 377–383.

(42) Jung, H.-J.; Malek, M. A.; Ryu, J.-Y.; Kim, B.; Song, Y.-C; Kim, H. K.; Ro, C.-U. *Anal. Chem.* **2010**, *82*, 6193–6202.

(43) Ryu, J.-Y.; Ro, C.-U. *Anal. Chem.* **2009**, *81*, 6695–6707.

(44) Song, Y.-C; Ryu, J.-Y.; Malek, M. A.; Jung, H.-J.; Ro, C.-U. *Anal. Chem.* **2010**, *82*, 7987–7998.

(45) Ro, C.-U.; Osan, J.; Van Grieken, R. *Anal. Chem.* **1999**, *71*, 1521–1528.

(46) Vekemans, B.; Janssens, K.; Vincze, L.; Adams, F.; Van Espen, P. *X-Ray Spectrom.* **1994**, *23*, 278–285.

(47) Ro, C.-U.; Osan, J.; Száloki, I.; de Hoog, J.; Worobiec, A.; Van Grieken, R. *Anal. Chem.* **2003**, *75*, 851–859.

(48) Ro, C.-U. *Powder Diffr.* **2006**, *21*, 140–144.

(49) Ro, C.-U.; Osán, J.; Száloki, I.; Oh, K. Y.; Van Grieken, R. *Environ. Sci. Technol.* **2000**, *34*, 3023–3030.

(50) Ro, C.-U.; Oh, K.-Y.; Kim, H. K.; Chun, Y.-S.; Osan, J.; de Hoog, J.; Van Grieken, R. *Atmos. Environ.* **2001**, *35*, 4995–5005.

(51) Spatial Resolution in ATR-FT-IR imaging: measurement and interpretation. Technical Note #007641_03; PerkinElmer, Inc.: Shelton, USA, 2006.

(52) Goldstein, J. I.; Newbury, D. E.; Joy, D. C.; Lyman, C.; Echlin, P.; Lifshin, E.; Sawyer, L.; Michael, J. *Scanning Electron Microscopy and X-ray Microanalysis*, 3rd ed.; Kluwer-Plenum: New York, 2003.

(53) Madejová, J.; Komadel, P. *Clays Clay Miner.* **2001**, *49*, 410–432.

(54) White, W. B. The carbonate minerals. In *The Infrared Spectra of Minerals*; Farmer, V.C., Ed.; Mineralogical Society: London, 1974; pp 227−284 (Monograph 4).

(55) Matteson, A.; Herron, M. M. *J. Sediment. Petrol.* **1993**, *63*, 1144–1148.

(56) Farmer, V. C. The layer silicates. In *The Infrared Spectra of Minerals*; Farmer, V.C., Ed.; Mineralogical Society: London, 1974; pp 331−363 (Monograph 4).

7977

dx.doi.org/10.1021/ac201956h |*Anal. Chem.* 2011, 83, 7970–7977